Journal of
Microscopy

Journal of Microscopy, Vol. 248, Pt 1 2012, pp. 90–101
Received 2 May 2012; accepted 16 July 2012

doi: 10.1111/j.1365-2818.2012.03654.x

Imaging nanometre-scale structure in cells using *in situ* aberration correction

C.J. FULLER & A.F. STRAIGHT
Department of Biochemistry, Stanford University School of Medicine, Stanford, California, U.S.A.

Key words. Aberration, centromere, colocalization, kinetochore, superresolution.

Summary

Accurate distance measurements of cellular structures on a length scale relevant to single macromolecules or macromolecular complexes present a major challenge for biological microscopy. In addition to the inherent challenges of overcoming the limits imposed by the diffraction of light, cells themselves are a complex and poorly understood optical environment. We present an extension of the high-resolution colocalization method to measure three dimensional distances between diffraction-limited objects using standard widefield fluorescence microscopy. We use this method to demonstrate that in three dimensions, cells intrinsically introduce a large and variable amount of chromatic aberration into optical measurements. We present a means of correcting this aberration *in situ* [termed 'Colocalization and *In-situ* Correction of Aberration for Distance Analysis' (CICADA)] by exploiting the fact that there is a linear relationship between the degree of aberration between different wavelengths. By labelling a cellular structure with redundantly multi-colour labelled antibodies, we can create an intracellular fiducial marker for correcting the individual aberrations between two different wavelengths in the same cells. Our observations demonstrate that with suitable corrections, nanometre scale three-dimensional distance measurements can be used to probe the substructure of macromolecular complexes within cells.

Introduction

The resolution of conventional light microscopy is limited by the diffraction of light to scales on the order of 100 nm. In most biological samples subcellular organization and structure ranges from the size of individual proteins to macromolecular complexes to organelles where relevant length scales span 1 nm–1 μm. Thus, the diffraction limit poses a significant barrier to interrogating cellular organization using light microscopy. In recent years, many techniques have been developed that circumvent this limit. These methods can be broadly categorized into reduction of the fluorescence excitation volume (Hell & Wichmann, 1994; Hell *et al.*, 1997), serial stochastic imaging of single molecules followed by image reconstruction (Betzig *et al.*, 2006; Rust *et al.*, 2006; Dani *et al.*, 2010), patterned illumination and interferometric methods (Gustafsson *et al.*, 1999; Gustafsson, 2000; Shao *et al.*, 2008) or imaging multiple separable wavelengths followed by registration and position estimation (Manders, 1997; Bornfleth *et al.*, 1998; Lacoste *et al.*, 2000; Michalet *et al.*, 2001; Churchman *et al.*, 2005; Warshaw *et al.*, 2005; Antelman *et al.*, 2009; Pertsinidis *et al.*, 2010; Hoyer *et al.*, 2011).

The use of multiple different wavelengths of light is particularly attractive for biological samples where it is desirable to know the real space distance between two populations of fluorescently labelled molecules or two parts of a single macromolecule. In practice, aberrations in even highly corrected microscope optics confound direct distance measurements unless the aberrations can be precisely determined and then corrected. Once these aberrations are corrected distance measurements accurate to several tens of nanometres are feasible (Manders, 1997; Bornfleth *et al.*, 1998).

It is currently possible to determine the locations of diffraction-limited fluorescent points to better than nanometre accuracy by applying modern fitting methods to the fluorescence emission profile (Thompson *et al.*, 2002; Yildiz *et al.*, 2003; Mortensen *et al.*, 2010). This increased accuracy of position estimation correspondingly increases the accuracy of aberration correction and distance measurements between different wavelength fluorescent molecules. The combined use of improved aberration correction and precise localization of different wavelength fluorescent molecules termed (single-molecule high-resolution colocalization (SHREC); Churchman *et al.*, 2005) provided a mechanism to measure

Correspondence to: Aaron F. Straight, 279 Campus Drive, Beckman Center B409A, Stanford, CA 94305, U.S.A. Tel: +650-723-2941; fax: +650-723-6783; e-mail: astraigh@stanford.edu

distances to ≈5 nm in two dimensions. SHREC was applied to observe the hand-over-hand stepping motions of single myosin motors *in vitro* (Churchman *et al.*, 2005; Nishikawa *et al.*, 2010) as well as mapping the organization of groups of centromere and kinetochore proteins in yeast (Joglekar *et al.*, 2009) and human (Wan *et al.*, 2009) cells.

In the previous studies that used SHREC or related approaches the distance calculation could be reduced to a two dimensional measurement problem by imaging a single in focus image plane. However, most biological samples are rich in three-dimensional information and thus require a method to measure three-dimensional distances between different wavelengths.

Cellular samples are optically complex. It has been observed that refractive index inhomogeneity within cells can lead to significant aberrations, which not only reduces resolution and signal amplitude (Gibson & Lanni, 1992; Schwertner *et al.*, 2004a,b), but can also lead to apparent position shifts of objects being imaged (Schwertner *et al.*, 2007). Although advanced adaptive-optics-based techniques have been developed to compensate for these aberrations in cells (Kam *et al.*, 2001; Ji *et al.*, 2010), measurement and correction of chromatic aberrations introduced by cells have remained relatively unexplored. These chromatic aberrations are a critical problem to address for quantitative multi-colour superresolution light microscopy in cells.

We present a method for correcting cellular aberration *in situ* by quantifying the local chromatic aberrations in cells using multiply fluorescently labelled antibodies emitting at different wavelengths. Using these multi-colour labels as fiducial marks we separately map the relationships between aberrations in different wavelengths. We show that in any given cell the amount of aberration between two wavelengths (e.g. green and red) is linearly related to the amount of aberration between two different wavelengths (e.g. green and far red), even though the magnitudes of the aberrations are not. Using the quantitative relationship between aberrations in different wavelength pairs we can correct for the cellular aberration between wavelengths. After applying these corrections, it is possible to map three-dimensional distances within cells to better than 10 nm accuracy.

Materials and methods

Sample preparation

Slides with multi-wavelength fluorescent beads were prepared from TetraSpeck 0.2 μm diameter fluorescent microspheres (Invitrogen) which were sonicated in a bath sonicator for 30 s on maximum power before use. 2 μL of the bead solution (as obtained from the manufacturer; reported concentration 2.3×10^{10} beads mL^{-1}) were spread onto a 18 mm square no. 1.5 H high-precision cover slip (Zeiss) using a pipet tip dipped into 0.2% triton X-100 (Sigma) (to break surface tension and allow even spreading onto the cover slip). After spreading over the surface, excess bead solution was wicked off the edge of the cover slip and the cover slip was air dried. Cover slips were mounted in 97% 2,2′-thiodiethanol (TDE)/3% phosphate-buffered saline (PBS, 137 mM NaCl, 2.7 mM KCl, 10 mM Na_2HPO_4, 2 mM KH_2PO_4, adjusted to pH 7.4 with HCl) (Staudt *et al.*, 2007), and sealed to a standard glass slide with nail polish.

Cell culture and immunofluorescence

HeLa cells were grown in Dulbecco's Modified Eagle Medium (DMEM), supplemented with 10% fetal bovine serum, penicillin and streptomycin, at 37°C under 5% CO_2. For immunofluorescence, cells were passaged directly onto untreated, ethanol-washed 18 mm square no. 1.5H cover slips (Zeiss) and allowed to recover for one day. Cells were arrested in 2 mM thymidine in Dulbecco's Modified Eagle Medium overnight, washed twice in Dulbecco's Modified Eagle Medium and released into fresh Dulbecco's Modified Eagle Medium for 9 h. Cells were fixed in PBS containing 2% formaldehyde, 10 mM ethylene glycol-bis-(2-aminoethyl)-N,N,N',N'-tetraacetic acid (EGTA), 4mM $MgCl_2$ and 0.5% triton X-100 for 5 min in a 37°C incubator, and then washed twice in PBS with 0.5% triton X-100.

The cells were washed twice in and blocked for at least 30 min in 150 mM NaCl, 20 mM tris-HCl pH 7.4, 0.1% triton X-100, 2% bovine serum albumin, 5% goat serum (Jackson Immunoresearch), 0.25 mg mL^{-1} casein (ABDIL). The primary antibodies were mouse monoclonal anti-Hec1 (Abcam, 9G3), used at 2 μg mL^{-1}, and rabbit polyclonal anti-CENP-T (Wan *et al.*, 2009), used at 1 μg mL^{-1}. Antibodies were diluted to their final concentration in ABDIL and hybridized to the cells for 1 h in ABDIL.

For experiments using multiply labelled secondary antibodies, unlabelled sheep anti-mouse antibody (Jackson Immunoresearch) was simultaneously conjugated with either AlexaFluor 488 NHS-ester and AlexaFluor 568 NHS-ester (Invitrogen) for a two-colour-labelled antibody, or these fluorophores as well as AlexaFluor 647 NHS-ester (Invitrogen) for a three-colour-labelled antibody. Labelled antibodies were purified over a G25 Sephadex column (Sigma) or a Bio-spin 6 column (Bio-rad) in PBS.

Secondary antibodies, Alexa-488/Alexa-568-conjugated sheep anti-mouse, used at 2 μg mL^{-1}, Alexa-488/Alexa-568/Alexa-647-conjugated sheep anti-mouse, used at 4 μg/mL, and Alexa-647-conjugated donkey anti-rabbit (Jackson Immunoresearch), used at 2 μg mL^{-1}, were diluted to final concentration in ABDIL and incubated with the cells for 1 h. Cells were washed 5 times in ABDIL and three times in PBS. Cover slips were exchanged into TDE-based mounting media in an series of increasingly concentrated solutions of TDE in PBS: 5 min in 10% TDE/90% PBS, 5 min in 25% TDE/75% PBS, 5 min in 50% TDE/50% PBS, then 5 min

each in two changes of 97% TDE/3% PBS (Staudt *et al.*, 2007). Excess mounting media from the exchange process was removed by gentle blotting with filter paper, and then cover slips were mounted in 97% TDE/3% PBS supplemented with 0.25 (w/v)% p-phenylenediamine, 5 (w/v)% n-propyl gallate and 0.25 (w/v)% 1,4-Diazabicyclo[2.2.2]octane (DABCO) and sealed to a standard glass slide with clear nail polish.

Microscopy

Imaging was performed on a Nikon Ti-E inverted microscope with a 100× 1.49 NA APO-TIRF lens (used for standard epifluorescence), using Nikon type NF immersion oil (n = 1.515 at 23°C). The microscope was enclosed in a plexiglass incubator temperature-controlled to 23.0 ± 0.1°C (*In Vivo* Scientific), and all samples were allowed to equilibrate to this temperature on the stage in contact with the oil and objective for at least 1 h before imaging. Samples were illuminated using a Lambda XL light source (Sutter Instruments), and wavelengths were selected with a quad-pass dichroic mirror (Chroma 89000); 490/20, 555/25 or 645/30 excitation filters (Chroma); and 525/36, 605/52 or 705/72 emission filters (Chroma). Images were acquired using an Andor iXon+ EMCCD camera model DU885 (8 μm pixel size) set for 20-fold EM gain and 13MHz readout and μ Manager software version 1.3 (Vale Lab, UCSF)(Edelstein *et al.*, 2010). Axial sectioning and movement used a piezo z-stage insert (Mad City Labs) with a 16-bit digital controller (Applied Scientific Instrumentation). Based upon calibration of the stage by the manufacturer, the limiting factor in the accuracy of the stage was the digitization from the controller (± 1.5 nm), and the accuracy and stability of the digital controller's output was verified using a voltage metre.

For imaging of fluorescent beads, we focused on the beads manually, and then sectioned through the beads using the piezo z-stage at 100 nm intervals over 2 μm, for a total of 21 sections per field, imaging each desired wavelength at each z-position. For imaging of cells, we used the same sectioning procedure, except for collecting 61 sections per field, over a total of 6 μm. We found that the Alexa488 fluorophore had both a fast-bleaching and slow-bleaching population under our imaging conditions. To avoid systematic apparent offset of this channel due to bleaching during sectioning, we pre-bleached the fast population by focusing in the middle of the sample and leaving the excitation light on for 30 s before beginning the sectioning. Typically, exposure times for cells were 1–2 s for 488 nm, 0.25 s for 568 nm and 1 s for 647 nm; collecting the full set of axial sections for a single field took 1–2 min for the beads, and 4–5 min for the cells.

Image processing

Objects in images were detected using custom-written java software previously used by our lab for segmentation and quantification of centromeres (Moree *et al.*, 2011). Segmentation quality was spot-checked by manually examining at least three randomly chosen images from each dataset; few errors were found, and these could be removed manually or automatically discarded during the subsequent fitting procedure. Source code and documentation for the segmentation software is freely available at http://straightlab.stanford.edu/software.

Colocalization analysis

The colocalization analysis was based upon that described previously for SHREC in two dimensions (Churchman *et al.*, 2005, 2006; Mortensen *et al.*, 2010). We used custom-written java software for the analysis; source code and documentation for the full colocalization procedure is freely available at http://straightlab.stanford.edu/software.

Localization

Every object identified using the segmentation software was fit to a gaussian in a 7 × 7 × 11 pixel by pixel by axial section box surrounding the maximum intensity pixel in the object using the maximum likelihood estimation with gaussian (MLEwG) procedure described in (Mortensen *et al.*, 2010). We used a photon-to-grey level conversion factor of 0.25 photons per grey level, taking into account the 80 000 electron full well capacity of the camera gain register (this would saturate before the detector area at our EM gain setting), the 20× EM gain and the 14bit digitization we used.

The fitting procedure used an initial guess of the x-y centroid of fluorescence over the 7 × 7 × 11 pixel box, and the brightest pixel in z at this centroid to start fitting the parameters of a three-dimensional gaussian function with constant background. We used seven fit parameters: amplitude, A; background, B; x-position, μ_x; y-position, μ_y; z-position, μ_z; x and y variance, $\sigma^2_{x,y}$, (constrained to have the same individual x and y variances and no covariance); and z-variance, σ^2_z. We optimized the likelihood of the intensity values in the box given a set of gaussian parameters using an optimization routine based on the Nelder–Mead downhill simplex method. The likelihood function, L, was defined as the product of the probability densities for the detected number of photons at each point in the fit box. The probability density for each pixel was a Poisson distribution with its mean equal to the value of the fitted gaussian at that pixel's position. Mathematically

$$L = \prod_i P(n_i; \lambda_i),$$

where i is an index over all pixels in the box to be fit, n_i is the detected photon count at the ith pixel, λ_i is the mean of the Poisson distribution for the ith pixel, given by the value of the gaussian function being fit at the location of the ith pixel,

(x_i, y_i, z_i):

$$\lambda_i = B + Ae^{-(((x_i-\mu_x)^2+(y_i-\mu_y)^2)/(2\sigma_{x,y}^2))-((z_i-\mu_z)^2/(2\sigma_z^2))}$$

and $P(n_i;\lambda_i)$ is the Poisson distribution

$$P(n_i;\lambda_i) = \frac{\lambda_i^{n_i} e^{-\lambda_i}}{n_i!}.$$

Aberration correction

We corrected for aberration in the microscope using a modification of the locally weighted mean mapping previously described (Churchman *et al.*, 2005; Goshtasby, 1988). The goal of this approach is to locally fit the aberration between two wavelengths to a second order polynomial at several fiducial points in the field of view of the microscope, and then to combine these local fits into a continuous global map of the aberration at any point in the field of view.

We used multi-wavelength fluorescent beads as fiducial markers to calculate and fit the aberration. In the original description of this approach, a single bead was translated through each position in the image, but because we desired both a large field of view and fine spatial sampling of the aberration, the number of images required to map the aberration was too great. As an alternative, we imaged many fields of beads randomly adhering to the cover slip, and combined these random fields into a single dataset, resulting in fine coverage of the full field of view.

As previously noted (Goshtasby, 1988), generating the locally weighted mean map with irregularly spaced markers can result in a failure to cover some points in the field. Furthermore, when calculating the polynomial fit to the aberration around a given point, a non-uniform distribution of beads may result in all of the nearby beads being used for correction positioned on one side of the point. This leads to accurate mapping on one side of this point, but potentially unrealistic mapping on the side lacking beads.

To circumvent this problem, we fit a larger number of neighbouring points using inexact polynomial fitting for each fiducial point. The procedure described in (Goshtasby, 1988) used a given fiducial and its five nearest neighbours to determine an exact fit. Instead we used 36 points total and performed a least-squares fit of the polynomial parameters. This had the advantage of making it less likely for all neighbouring points to lie to one side of a given fiducial point, as well as producing fits that were less sensitive to error in any one data point. In practice, we found that the registration error associated with this procedure was relatively invariant with the number of points used for the fit over a range from 18 to 72. We chose the number 36 because it produced minimal registration error across several test datasets.

We performed this 36-point fit at each bead in the correction dataset. (We refer to each bead as the 'origin' of its corresponding 36 point local aberration fit.) We then used this dataset to correct points in the experimental dataset using a previously described weighting function (Goshtasby, 1988). Briefly, for a point in the experimental dataset, its correction is calculated by summing the correction from every local aberration fit, weighted by the distance to the origin of that fit. The closer the experimental point to the origin of that fit, the more highly weighted that fit is. The exact form of the weighting function ensures that such a weighting scheme gives a continuous map of aberration across the entire field. Mathematically, at a given point, the total correction C is the normalized sum of the correction from each polynomial, C_i, over every polynomial fit in the correction dataset

$$C = \frac{\sum_i W_i C_i}{\sum_i W_i},$$

where W_i is the weight of the ith polynomial, given by

$$W_i = 1 - 3R^2 + 2R^3 \quad 0 \le R \le 1$$
$$W_i = 0 \quad \text{elsewhere.}$$

R is a normalized distance between the point in the experimental dataset being corrected and the origin of the ith polynomial fit

$$R = ((x - x_i)^2 + (y - y_i)^2)^{(0.5)}/R_{36},$$

where x_i and y_i are the position of the origin of the ith polynomial fit, and x and y are the position of the point in the experimental dataset that is being corrected. R_{36} is the distance from the origin of the ith local aberration fit to the furthest point used in generating that fit. Normalization by R_{36} ensures that the influence of any local aberration fit does not extend beyond the range of data used to calculate that fit.

We compute such a weighted correction for each dimension separately as a function of the x–y position in the field of view.

Error assessment

We calculate the fit error in the position of each object following the treatment in (Mortensen *et al.*, 2010) for the Maximum Likelihood Estimation with Gaussian method (MLEwG), extending it to three dimensions. For the case of the beads, the error was dominated by photon counting noise, but for measurements in cells, background noise was significant and had to be considered.

We model the PSF, $P(\mathbf{r}) = P(x, y, z)$, as a three-dimensional normalized gaussian with a x and y variance the same, σ^2, and distinct z variance, ρ^2

$$P(x, y, z|\mu, \sigma^2, \rho^2) = \frac{1}{2\sqrt{2}\sigma^2\rho\pi^{3/2}} e^{-(((x-\mu_x)^2+(y-\mu_y)^2)/(2\sigma^2))-((z-\mu_z)^2/(2\rho^2))}.$$

Pixel size. To establish the error due to pixel size, we first integrate over the volume of a pixel

$$p_i = \int_{\text{pixel i}} P(x, y, z)\, dx\, dy\, dz.$$

We expand to second order about the centre of the pixel, $\mathbf{r_i} = (x_i, y_i, z_i)$ (first-order terms and mixed second-order terms vanish in the integral)

$$p_i \approx \int_{-\alpha/2}^{\alpha/2}\int_{-a/2}^{a/2}\int_{-a/2}^{a/2}\left[P(\mathbf{r_i}) + \frac{x^2}{2}\frac{\partial^2 P}{\partial x^2}(\mathbf{r_i}) + \frac{y^2}{2}\frac{\partial^2 P}{\partial y^2}(\mathbf{r_i}) + \frac{z^2}{2}\frac{\partial^2 P}{\partial z^2}(\mathbf{r_i})\right] dx\, dy\, dz.$$

Let a = the pixel size in x–y and α = the pixel size in z. Then, evaluating the derivatives on the 3D Gaussian, performing the integrals and simplifying, yields

$$p_i = a^2\alpha P(\mathbf{r_i})\left[1 + \frac{a^2}{12\sigma^2}\left(\frac{(x-\mu_x)^2 + (y-\mu_y)^2}{2\sigma^2} - 1\right) + \frac{\alpha^2}{12\rho^2}\left(\frac{(z-\mu_z)^2}{2\rho^2} - \frac{1}{2}\right)\right].$$

As for the two-dimensional case in (Mortensen *et al.*, 2010), we note that defining $\sigma_a^2 = \sigma^2 + \frac{a^2}{12}$ and $\rho_\alpha^2 = \rho^2 + \frac{\alpha^2}{12}$ allows us to express this result (to same order in $\frac{a}{\sigma}$ and $\frac{\alpha}{\rho}$) as

$$p_i = a^2\alpha P\left(\mathbf{r_i}|\mu, \sigma_a^2, \rho_\alpha^2\right). \quad (1)$$

We use this form for the subsequent analysis, dropping the subscripts on σ_a^2 and ρ_α^2, so that henceforth σ^2 and ρ^2 will refer to these pixel-size-modified variances.

Background noise. The expected number of photon counts in pixel i, E_i, is

$$E_i = Np_i + b^3,$$

where N is the total number of photons originating from the object being analysed, p_i is the normalized point spread function in the ith pixel calculated in equation (1), and b^3 is the (assumed constant) expected photon count due to background in a three-dimensional pixel.

Let $\Delta\theta$ be the deviation of the value of a parameter from its true value. To find the localization precision, we then want to calculate $\langle(\Delta\theta)^2\rangle$, that is, the variance of the parameter estimate, for θ equal to each of the mean positions of the Gaussian fit, μ_x, μ_y, μ_z.

From (Mortensen *et al.*, 2010), these estimates are given by

$$\langle(\Delta\mu_j)^2\rangle = 1 \Bigg/ \left(\sum_i \frac{\left(\frac{\partial E_i}{\partial\mu_j}\right)^2}{E_i}\right),$$

where i is the pixel index, and j refers to one of x, y or z.

To calculate the sum over pixels, we replace it by an integral over space

$$\langle(\Delta\mu_j)^2\rangle = 1 \Bigg/ \left(\int \frac{\left(\frac{\partial\left(Np(\mathbf{r}) + \frac{b^3}{a^2\alpha}\right)}{\partial\mu_j}\right)^2}{Np(\mathbf{r}) + \frac{b^3}{a^2\alpha}}\, dx\, dy\, dz\right).$$

We can take advantage of symmetry in computing this integral by considering the quantity

$$\int \frac{\left(\frac{\partial(Np(\mathbf{r}))}{\partial\boldsymbol{\mu}}\right)^2}{Np(\mathbf{r}) + \frac{b^3}{a^2\alpha}}\, dx\, dy\, dz = \int \frac{\left(\frac{\partial(Np(\mathbf{r}))}{\partial\mu_x}\right)^2 + \left(\frac{\partial(Np(\mathbf{r}))}{\partial\mu_y}\right)^2 + \left(\frac{\partial(Np(\mathbf{r}))}{\partial\mu_z}\right)^2}{Np(\mathbf{r}) + \frac{b^3}{a^2\alpha}}\, dx\, dy\, dz.$$

Splitting the three terms and calculating the derivatives yields

$$\frac{N}{\sigma^4}\int \frac{(p(\mathbf{r}))^2(x-\mu_x)^2}{p(\mathbf{r}) + \frac{b}{Na^2}} dx\, dy\, dz + \frac{N}{\sigma^4}\int \frac{(p(\mathbf{r}))^2(y-\mu_y)^2}{p(\mathbf{r}) + \frac{b}{Na^2\alpha}} + \frac{N}{\rho^4}\int \frac{(p(\mathbf{r}))^2(z-\mu_z)^2}{p(\mathbf{r}) + \frac{b}{Na^2\alpha}}\, dx\, dy\, dz.$$

We change variables using $\zeta = \frac{\sigma}{\rho}z$ and $\mu_\zeta = \frac{\sigma}{\rho}\mu_z$:

$$\frac{N\rho}{\sigma^5}\int \frac{(p(\mathbf{r}))^2(x-\mu_x)^2}{p(\mathbf{r}) + \frac{b}{Na^2\alpha}}\, dx\, dy\, d\zeta + \frac{N\rho}{\sigma^5}\int \frac{(p(\mathbf{r}))^2(y-\mu_y)^2}{p(\mathbf{r}) + \frac{b}{Na^2\alpha}}\, dx\, dy\, d\zeta + \frac{N}{\rho\sigma^3}\int \frac{(p(\mathbf{r}))^2(\zeta-\mu_\zeta)^2}{p(\mathbf{r}) + \frac{b}{Na^2\alpha}}\, dx\, dy\, d\zeta.$$

This substitution makes

$$p(x, y, \zeta) = \frac{1}{2\sqrt{2}\sigma^2\rho\pi^{3/2}} e^{-(((x-\mu_x)^2 + (y-\mu_y)^2 + (\zeta-\mu_\zeta)^2)/(2\sigma^2))},$$

and because this is now symmetric with respect to x, y and ζ, we can conclude that the integral must be the same in each term.

Therefore,

$$\langle(\Delta\mu_j)^2\rangle = 1 \Bigg/ \left(c_j N \int \frac{\left(\frac{\partial(p(\mathbf{r}))}{\partial\boldsymbol{\mu}}\right)^2}{p(\mathbf{r}) + \frac{b^3}{a^2\alpha N}}\, dx\, dy\, dz\right), \quad (2)$$

where $c_x = c_y = \frac{\rho^2}{2\rho^2+\sigma^2}$ and $c_z = \frac{\sigma^2}{2\rho^2+\sigma^2}$.

Consider now just the integral portion of Eq. (2), expressed in cylindrical coordinates

$$\int \frac{r\left(\frac{\partial(p(r,\theta,z))}{\partial\boldsymbol{\mu}}\right)^2}{p(r,\theta,z) + \frac{b^3}{a^2\alpha N}}\, dr\, d\theta\, dz = 2\pi\int\left(\frac{1}{\sigma^4}\frac{r^3p^2}{p + \frac{b^3}{a^2\alpha N}} + \frac{1}{\rho^4}\frac{rz^2p^2}{p + \frac{b^3}{a^2\alpha N}}\right) dr\, dz. \quad (3)$$

First performing the integrals over r, the first term in Eq. (3) must be integrated numerically, but can be put into a simpler form, as in the treatment in (Mortensen *et al.*, 2010) using the substitution $\log(R) = \frac{-r^2}{2\sigma^2}$. In addition, we define $A = \frac{1}{2\sqrt{2}\pi^{3/2}\rho\sigma^2}$ and $B = B(z) = Ae^{-z^2/(2\rho^2)}$.

$$\int \frac{1}{\sigma^4}\frac{r^3p^2}{p+\frac{b^3}{a^2\alpha N}}\,dr = -2B\int_{R=0}^{R=1}\frac{R\log(R)}{R+\frac{b^3}{Ba^2\alpha N}}\,dR.$$

Defining $\mathcal{I}_1(\tau) = -\int_0^1 \frac{t\log(t)}{t+\tau}dt$ as in (Mortensen *et al.*, 2010) yields

$$\int \frac{1}{\sigma^4}\frac{r^3p^2}{p+\frac{b^3}{a^2\alpha N}}\,dr = 2B\mathcal{I}_1\left(\frac{b^3}{Ba^2\alpha N}\right). \quad (4)$$

The integral over r of the second term in Eq. (3) can be evaluated analytically using the same substitution with R and B

$$\begin{aligned}\int \frac{1}{\rho^4}\frac{rz^2p^2}{p+\frac{b^3}{a^2\alpha N}}\,dr &= \frac{z^2\sigma^2B}{\rho^4}\int_{R=0}^{R=1}\frac{R}{R+\frac{b^3}{Ba^2\alpha N}}\,dR \\ &= \frac{z^2\sigma^2B}{\rho^4}\left(1-\frac{b^3}{Ba^2\alpha N}\log\left(1+\frac{Ba^2\alpha N}{b^3}\right)\right). \quad (5)\end{aligned}$$

Now we take the integrals over z. The expression in Eq. (4), which is already being evaluated numerically over r, must also be numerically evaluated over z

$$\int 2B\mathcal{I}_1\left(\frac{b^3}{Ba^2\alpha N}\right)dz. \quad (6)$$

The first term of Eq. (5) can be evaluated analytically

$$\frac{\sigma^2}{\rho^4}\int z^2B\,dz = \frac{(2\pi)^{1/2}\sigma^2A}{\rho}. \quad (7)$$

The second term of Eq. (5) must also be evaluated numerically

$$\frac{\sigma^2b^3}{\rho^4a^2\alpha N}\int -z^2\log\left(1+\frac{Ba^2\alpha N}{b^3}\right)dz. \quad (8)$$

Combining the expressions from Eqs (6), (7) and (8), and putting them into Eq. (2) yields a complete expression for the variance of the position estimates

$$\langle(\Delta\mu_j)^2\rangle = \left[2c_jN\pi\left(\frac{(2\pi)^{1/2}\sigma^2A}{\rho}+\frac{\sigma^2b^3}{\rho^4a^2\alpha N}\int -z^2\log\left(1+\frac{Ba^2\alpha N}{b^3}\right)dz+\int 2B\mathcal{I}_1\left(\frac{b^3}{Ba^2\alpha N}\right)dz\right)\right]^{-1}.$$

We used these expressions for variance (times an additional factor of two due to excess noise resulting from the EMCCD (Mortensen *et al.*, 2010)) to calculate our localization precision for both beads and cells. We also calculate the target registration error, a measure of how well the aberration can be corrected, according to the procedure in (Churchman *et al.*, 2005). For images of cells, we discarded kinetochores whose localization error from all three channels combined in quadrature was greater than a cutoff, which we set at 15 nm.

Distance measurements

To confirm that we could accurately measure axial distances between objects offset from each other that are labelled in two different wavelengths, we axially sectioned through fields of fluorescent beads just as we had done to acquire the datasets used for aberration correction, but between imaging the first wavelength and the second wavelength, we also translated the z-stage by a known amount (0, 10, 20 or 30 nm). We imaged the first wavelength again after each translation to assess the combined error of the fitting procedure and the movement of the stage.

After correction for aberration (or in the case of the control comparison between the offset images using the same wavelength, with no correction), we obtained a distribution of distances between the beads before and after the offset, and we fit (using a robust maximum likelihood method, which imposes a minimum probability density for any parameter value, with a Nelder–Mead downhill simplex optimizer) this to the p_{3D} distribution described in (Churchman *et al.*, 2006)

$$p_{3D}(r) = \sqrt{\frac{2}{\pi}}\frac{r}{\sigma\mu}e^{-\frac{\mu^2+r^2}{2\sigma^2}}\sin h\left(\frac{r\mu}{\sigma^2}\right),$$

where r is one of the distances measured, μ is the separation between objects imaged in the two different wavelengths, and σ is the uncertainty in the position, which we allowed to be fit as well, as we had no *a priori* way to estimate the uncertainty due to biological variability.

Measurement and correction of chromatic aberration within cells

To measure chromatic aberration within cells, we used multiply labelled secondary antibodies along with a primary mouse anti-Hec1 antibody. After correcting for aberration in the microscope optics using the bead slides as described, we sectioned through cells stained with anti-Hec1 and a triply labelled secondary antibody. The remaining separation between the positions of each triply labelled centromere in each wavelength we termed the cell-induced aberration at that centromere. To parametrize the relationship between the cell-induced aberration in the different wavelength pairs, we performed a robust linear fit (using the MATLAB function `robustfit` with constant term disabled) of the cell-induced aberration between 525 and 705 nm emission versus the aberration between 525 and 605 nm emission. We performed a single fit using pooled data from all repeats of this measurement across several days for each of the x, y and z dimensions, and then used these fit parameters for correction of all subsequent datasets.

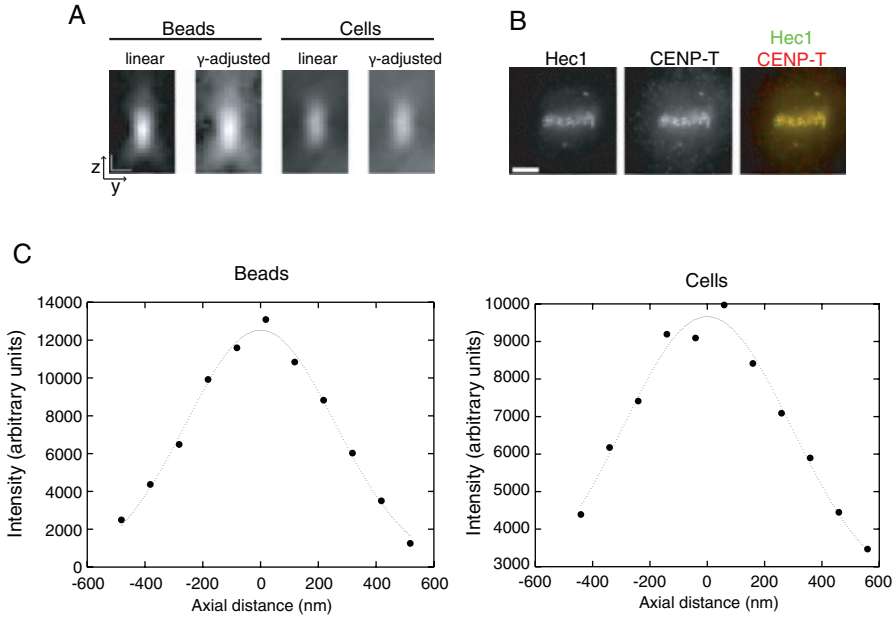

Fig. 1. *A. Point spread functions:* A y–z view of a bead and a centromere stained for Hec1 are shown both linearly scaled and γ-adjusted to show the faint portions of the images. Bar: 0.4 μm for both y and z (the pixel size for y and z is not the same). *B. Immunofluorescence images:* A single plane image is shown for a HeLa cell stained with anti-Hec1 and anti-CENP-T. Left to right: Hec1, CENP-T, Hec1 (green)/CENP-T (red) merge. Bar: 5 μm. *C. Gaussian fits to the axial dimension:* The central 1.1 μm of the intensity profile along the axial dimension through a bead and a centromere stained for Hec1 are plotted versus the position from the centre of the intensity distribution (black circles). The gaussian fit to each intensity profile is shown (dotted line). For the bead profile, $R^2 = 0.99$; for the centromere profile, $R^2 = 0.98$.

For measurements of interprotein distances in cells, we used primary anti-Hec1 and anti-CENP-T antibodies, and a double-labelled secondary recognizing the anti-Hec1 and a single-labelled secondary recognizing the anti-CENP-T. We measured the cell-induced aberration at each centromere (after correction using beads) using the 525 and 605 nm emission from the double-labelled secondary, applied the linear parameters determined earlier to estimate the aberration between 525 and 705 nm emission at each centromere, and then used this as a correction to measure the distance between Hec1 and CENP-T at each centromere. For experiments involving stage offsets and triple-labelled Hec1, we applied the same correction procedure used for the CENP-T labelling to the 705 nm channel of the triple-labelled Hec1, which had been offset using the piezoelectric stage.

Results

To develop a method for measuring nanometre-scale three-dimensional distances in cells we faced two primary challenges. The first was to extend the high-resolution colocalization approach to three dimensions and the second was to develop an method for correcting additional aberrations introduced by cells. To extend the SHREC technique to three dimensions we first had to correct the three-dimensional aberration in the optical system. We collected axial sections through samples (200 nm fluorescent beads) at 100 nm intervals using a piezoelectric stage and then fit a three-dimensional Gaussian function to the resulting image stack for each object to determine its position. Sample point spread functions as well as gaussian fits to the axial dimension are shown in Figure 1. By collecting datasets of 20 random fields of fluorescent beads, for a total of about 500 beads over the 256×256 pixel image area, we mapped the magnitude of the aberration as a function of position in the field of view in all three dimensions and then corrected the aberration in three dimensions (Figure 2A).

We calculated the target registration error (Churchman *et al.*, 2005), a measure of how completely aberration has been corrected, using five independently acquired sets of corrections. Our measured TRE was 5.2 ± 0.1 nm (mean $\pm$ SEM) setting the approximate lower bound of measurable distances with our procedure and equipment. We collected $8.4 \times 10^4 \pm 1.2 \times 10^4$ and $8.0 \times 10^4 \pm 0.8 \times 10^4$ (mean $\pm$ SD of all measurements from one representative dataset) photons for each bead from the combined image stack in the 525 and 605 nm channels, respectively. This corresponded to an error associated with the position fitting, 1.9 ± 0.2 nm for the 525 nm channel and 2.1 ± 0.1 nm for the 605 nm channel (mean $\pm$ SD of all measurements from one representative dataset), which was small in comparison to the registration error. We do not expect that other localization approaches that could achieve higher accuracy, such as fitting a full 3D PSF, would significantly improve the overall error because

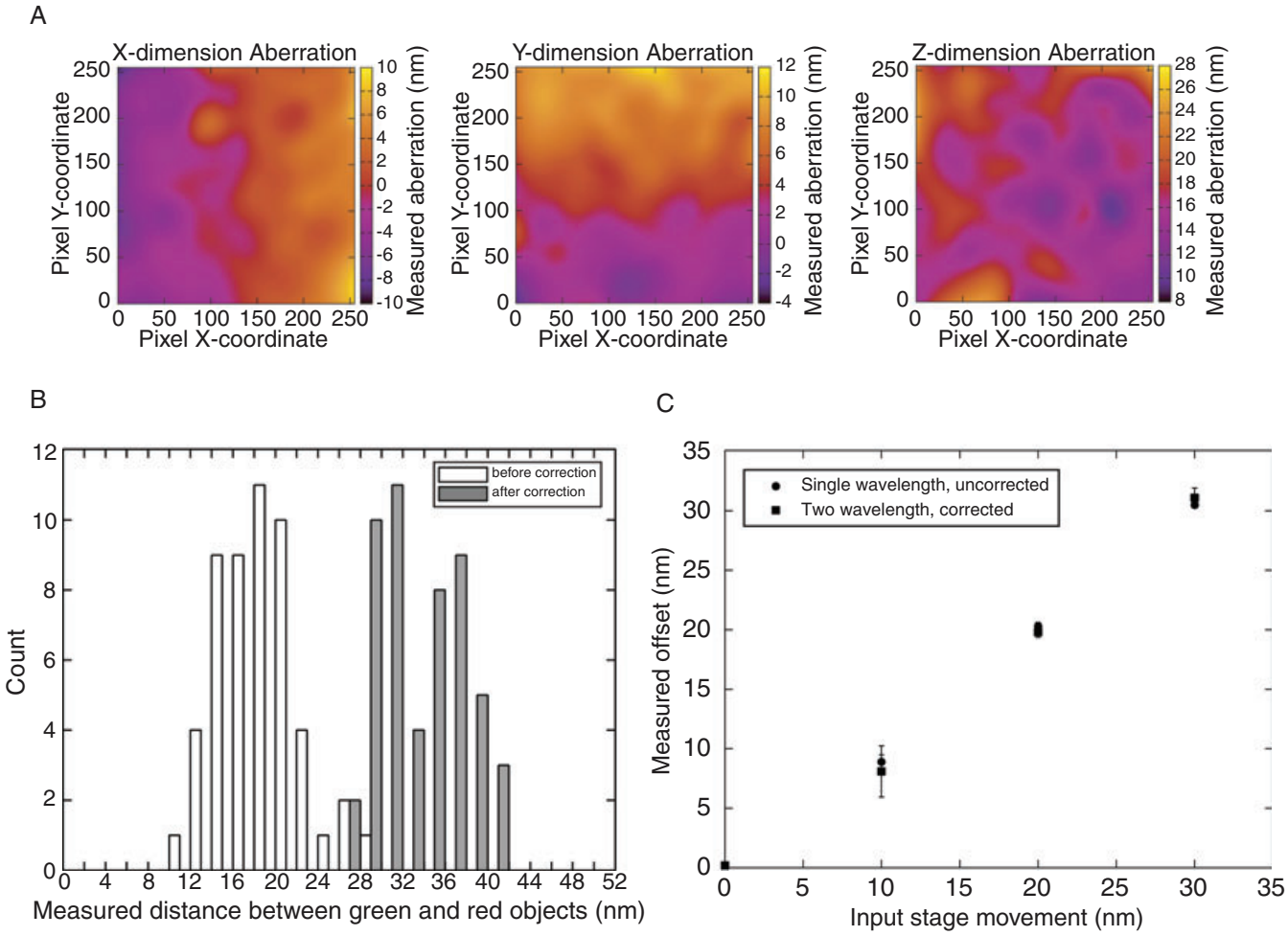

Fig. 2. *A. Maps of aberration in three dimensions:* The aberration correction, sampled at each pixel in the field of view, is plotted as a heatmap separately for each dimension. The magnitude of the aberration is indicated by the colour axis, which is scaled independently for each dimension. *B. Histograms of measured distances for 30 nm bead offset:* Apparent three-dimensional distances between each bead's image in the 525 and 605 nm wavelengths were calculated and plotted as a histogram both before correction for aberration (white) and after correction (grey). *C. Measured bead offsets as a function of input offsets:* The measured offset distance between the first 605 nm image and the 525 nm image after aberration correction (grey) as well as the (uncorrected) measured offset distance between the first 605 nm image and the second 605 nm image (white) are plotted as the mean ± SEM of five independent correction and measurement datasets for each stage offset.

the fitting error is already smaller than the registration error. Accordingly, decreasing the fitting error by a factor of two by increasing the photon count did not measurably decrease the registration error.

Before applying this technique in cells, we verified that it was possible to accurately measure three dimensional distances between different wavelengths *in vitro*. To do this, we needed a distance standard where labels in different wavelengths were separated by a known amount in three dimensions. We generated such a distance standard by imaging multi-wavelength fluorescent beads in two wavelengths, and using precise movement of a piezoelectric stage to offset the axial position of the beads between the acquisition of each wavelength. This had the effect of making the apparent position of the beads in one wavelength be offset from the other by the known distance the piezoelectric stage was moved. We imaged multi-wavelength fluorescent beads at 605 and 525 nm by first imaging the beads at 605 nm then moving the stage a short axial distance (0, 10, 20 or 30 nm) followed by imaging the 525 nm wavelength. We measured the apparent distances between beads in the two channels before and after correcting for aberration, and then fit the resulting distributions of distances (see Methods) to determine the separation between objects in the two wavelengths. Histograms of the distributions of distances are plotted in Figure 2(B) for a single experiment with 30 nm offset between wavelengths. To test the repeatability of our distance measurements and to control for inaccuracies in the stage

movement we repeated the image collection of fluorescent beads with a defined offset but we acquired 605 and 525 nm wavelength images both before and after the offset. The images of the beads taken in the same wavelength before and after the offset allowed us to test the accuracy of the stage movement without complications from the aberration and correction procedure.

We repeated this procedure five times and measured the 0, 10, 20 and 30 nm offsets between the two wavelengths to be 0.2 ± 0.1 nm, 8 ± 2 nm, 19.8 ± 0.4 nm and 31.1 ± 0.8 nm (mean $\pm$ SEM, n=5 cover slips, each independently corrected for aberration) respectively after correction for aberration. The same measurements taken between two offset images in a single wavelength (605 nm) were 0.24 ± 0.04 nm, 8.9 ± 0.6 nm, 20.3 ± 0.3 nm and 30.5 ± 0.3 nm for the 0, 10, 20 and 30 nm offsets, respectively (Figure 2C).

The optical environment of the cell is considerably more complex than that surrounding beads stuck to a cover slip, and it was unclear whether additional cellular aberrations would be a significant source of error in our measurements. The kinetochore is a multi-protein complex responsible for the attachment of eukaryotic chromosomes to the mitotic spindle in mitosis and many interprotein distances at the kinetochore have been previously measured in one dimension (Wan, 2010). Thus, we used labelled kinetochores as a system to estimate the degree of aberration induced by the cell in three dimensions. To generate fiducial marks in cells we redundantly labelled the kinetochore protein Hec1 using indirect immunofluorescence with a secondary antibody conjugated to green and far red fluorophores. We then repeated the same stage offset experiment in Figure 2 but using kinetochores rather than beads. We sectioned through cells at 100 nm intervals, and at each section, imaged the cell in green, offset the stage by 15, 20, 40 or 60 nm axially, and then imaged the cell in far red. After correction the system for optical aberration using a bead cover slip affixed to the same slide, we measured the stage offset using the green and far red channels from the images of the cell. We measured 29 ± 17 nm, 20 ± 2 nm, 15 ± 6 nm and 16 ± 10 nm (mean $\pm$ SEM, $n = 3$ for 15 and 60 nm offsets, $n = 4$ for 20 and 40 nm offsets), for the 15, 20, 40 and 60 nm distances, respectively (Figure 3A). Therefore, we concluded that the aberration introduced by cells is systematic and not negligible for three dimensional high-resolution colocalization.

To quantify the cellular aberration, we measured the apparent distance between green and far red in cells without moving the stage such that the green and far red signals should be in the same location. We observed a systematic offset of median 49 nm in the positive z direction (indicating that the position of the far red image was further into the sample). The offsets in x and y were within noise. Moreover, when we assessed the variability of this aberration within cells versus between cells (Figure 3C), we found that in general the variation between cells (standard deviation of median aberration value for each cell = 20 nm, n = 37 cells) could not be explained by the variation within cells (median absolute deviation/sqrt(n) for all centromeres within each cell = 5 nm on average, n varies depending on the number of fittable centromeres in each cell). This indicated that the amount of chromatic aberration introduced by cells was variable from cell to cell. Although this aberration varied with depth into the sample, the reported chromatic dispersion of the mounting media (Staudt *et al.*, 2007) is too small to account for this effect. Therefore, this aberration is an intrinsic property of each cell, and to make reliable three-dimensional cellular measurements it is necessary to correct for the aberration in each cell.

To correct the cellular aberration we required a fiducial mark in each cell that could be used for aberration correction before making a distance measurement. We determined whether we could generate such a fiducial mark by labelling a kinetochore protein (Hec1) with a triply labelled secondary antibody and determining whether the aberration between two wavelengths (e.g. green and red) could be used to predict the aberration between two different wavelengths (e.g. green and far red) at the same point. We quantified the relationship among aberrations at different wavelengths by repeating the imaging of the cells using a triply labelled secondary antibody (green, red, far red). When we plotted the aberration after bead correction between the green and far red channels (525 and 705 nm emission) versus the aberration between the green and red channels (525 and 605 nm emission) we observed a linear relationship over the range of aberrations seen in our cells (Figure 3D). A linear fit (with no constant term) to these aberrations in the z-direction yielded a slope of 1.33 ± 0.03 (95% CI), and $R^2 = 0.53$. We then asked whether we could correct the aberration between the green and far red wavelengths using this linear fit and the value of the aberration between the green and red wavelengths. We corrected each kinetochore in each cell by measuring the cell-induced aberration between the green and red channels in z, multiplying by the slope, and subtracting this value from the cell-induced aberration between green and far red. (We also performed the analogous procedure for x and y aberrations, but these were so small in comparison that it did not have a significant effect.) After applying this correction, we found that though there was still some variation from cell to cell, the aberration was distributed around zero to within noise (7 ± 19 nm median $\pm$ m.a.d. over all kinetochores in all cells). Thus, by using this multi-wavelength correction in cells we could gain additional accuracy in our estimation of axial position (Figure 3C). We expect that any residual offset from zero here will bound the accuracy of the method, as this could be systematic error. Therefore, we claim that the potential accuracy of the technique in this case is 7 nm.

This cellular aberration correction procedure should now enable accurate distance measurements in cells. To verify

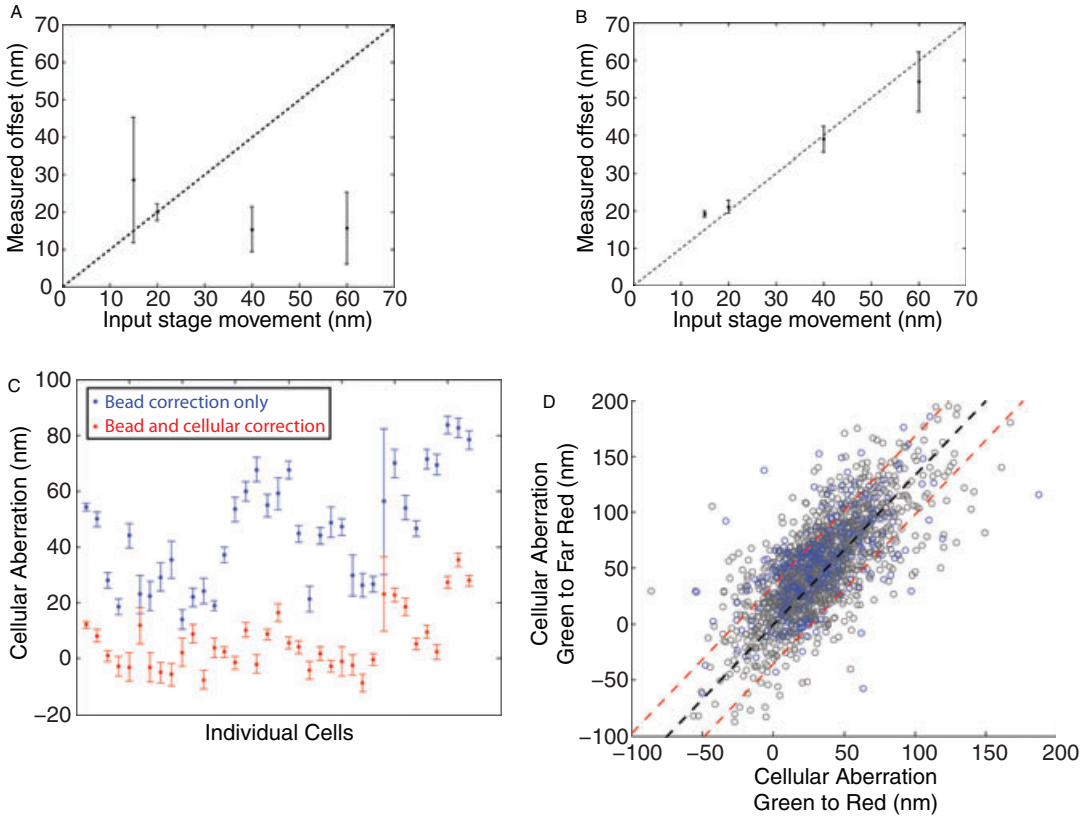

Fig. 3. *A. Measured cell offsets as a function of input offsets:* The measured offset distance between the 705 nm image and the 525 nm image after aberration correction with beads is plotted as the mean ± SEM of three (15, 60 nm offset) or four (20, 40 nm offset) independent correction and measurement datasets for each stage offset. The dotted line indicates a slope of 1. *B. Measured cell offsets as a function of input offsets after cellular correction:* The measured offset distance between the 705 nm image and the 525 nm image, after aberration correction with beads and cellular correction using the measured aberration between the 605 and 525 nm images, is plotted as the mean ± SEM of three (15, 60 nm offset) or four (20, 40 nm offset) independent correction and measurement datasets for each stage offset. The dotted line indicates a slope of 1. *C. Comparison of aberration within cells and among cells:* The median aberration between 525 and 705 nm wavelengths remaining after correction using beads alone (blue) or beads and the cellular correction (red) is plotted for 37 individual cells (taken from four separate slides from multiple different days). Error bars denote the median absolute deviation of all kinetochores in a cell divided by the square root of the number of kinetochores in that cell. The number of kinetochores per cell varies depending on how many kinetochores were widely enough separated from other kinetochores to be fit reliably. *D. Relationship between chromatic aberration in different wavelength pairs:* The measured difference between the z positions of all kinetochores in the 525 and 705 nm images is plotted versus the measured z offset of the same kinetochores in the 525 and 605 nm images. Points in blue denote all the kinetochores from one of the same 37 cells in (C). The black dashed line denotes the linear fit to the data. The red dashed line indicates ± 1 SD of all points in the direction perpendicular to the linear fit. 15 points (<1% of the total) lie outside the bounds of the graph, which were chosen to maximize the visibility of the bulk of the data, but these points were included in the fit.

this, we repeated the stage offset experiment in three-colour-labelled cells, first correcting the optical system aberration using beads, then correcting the cell-induced aberration between green and red to estimate the aberration between green and far red, and finally measuring the stage offset using green and far red corrected. We measured 18.8 ± 0.9 nm, 21 ± 2 nm, 39 ± 4 nm and 54 ± 8 nm (mean ± SEM, n = 3 for 15 and 60 nm offsets, n = 4 for 20 and 40 nm offsets) for the 15, 20, 40 and 60 nm distances, respectively (Figure 3B). The disagreement at the 15 nm distance likely reflects that with this antibody and wavelength combination our combined fitting and registration error is between 15 and 20 nm. This error is normally random, not systematic, but for distances less than or equal to the scale of this error, the fitting procedure cannot distinguish those distances from a distance approximately equal to the fitting error. This reflects the lower limit of measurable distances. It may be possible to reduce this limit with staining reagents that give higher signal and lower background and therefore lower fitting error. Distances larger than this limit are not subject to systematic error, and can therefore be measured to desired precision with additional collection of data.

The previous measurements of one-dimensional human kinetochore organization used a clever method termed the

'Delta method' that eliminates the need for aberration correction by taking advantage of the fact that at metaphase, kinetochores on linked sister chromatids are paired. By measuring the distance between paired kinetochores for two different kinetochore proteins and projecting those distances onto a single dimension, the distance between proteins in an individual kinetochore can be determined by calculating the difference. However, this method is limited to measuring distances along the axis between sister kinetochores.

To determine whether we could use our extension of SHREC to probe cellular structures in three dimensions we measured the separation between the centromere and kinetochore proteins CENP-T and Hec1. Although there are several of each of these proteins at a single centromere, they localize to a volume smaller than the diffraction limit of our system, so it is possible to localize the centroid of the distribution of these molecules precisely.

In cells at metaphase, the projected distance between the centroids of CENP-T and Hec1 fluorescence in paired kinetochores had been previously measured as 59 ± 1 nm (mean $\pm$ SEM) using the Delta method (Wan *et al.*, 2009). We repeated this measurement using the Delta method on our cells and found the Hec1-CENP-T distance to be 56 ± 1 nm. We applied our technique to metaphase HeLa cells stained for Hec1 and CENP-T using the same antibodies and conditions as the previous study that used the Delta method (Wan *et al.*, 2009). We measured the CENP-T/Hec1 distance as 62 ± 3 nm (mean $\pm$ SEM, n = 3 cover slips), indicating that the centroid of CENP-T lies close to the axis between sister kinetochores defined by Hec1.

Discussion

We have demonstrated a method for accurately measuring three-dimensional distances to precision better than 10 nm between diffraction-limited fluorescent objects in different wavelengths. When applied to distance measurements between kinetochore proteins, our method agrees extremely well with the result obtained from the Delta measurement.

The three-dimensional measurement approach we have described should help to bridge the gap between short-range cellular measurement techniques like fluorescence resonance energy transfer and more conventional measurements using light microscopy above the diffraction limit. It has the distinct advantage of three dimensionality without requiring any specialized equipment beyond a standard epifluorescence microscope equipped with an accurate motorized stage and should complement other existing superresolution imaging methods. This method should be readily applicable to distance measurements on fixed or static biological samples and should facilitate high resolution quantitative studies of macromolecular organization in cells.

We have also shown using this method that cells themselves introduce a large amount of chromatic aberration in the axial direction of the microscope. This finding implies that any multi-colour measurement in three dimensions in a cell by any technique must account for this effect to avoid systematic error in the results. We presented a means for correcting this aberration in every cell (and in our case at every point of interest) by using redundant multi-colour immunolabelling as a fiducial mark to measure the aberration, and then using the relationship between aberrations in different wavelengths to infer and correct the aberration at the wavelength used to make the measurement. We have used this aberration correction as part of three-dimensional high-resolution colocalization. This same method of correction could be used to enhance any superresolution or diffraction limited microscopy modality.

Acknowledgements

We gratefully acknowledge Ted Salmon, Xiaohu Wan, Jim Spudich, Kim Mortensen, Jongmin Sung, Mary Elting, Charles Limouse and Michelle Rengarajan for helpful advice. This work was supported by the National Institutes of Health (GM074728 and RR026775) to AFS and by the Stanford Bio-X Interdisciplinary Initiatives Program. CJF was supported by a Gerald J. Lieberman fellowship.

References

Antelman, J., Wilking-Chang, C., Weiss, S. & Michalet, X. (2009) Nanometre distance measurements between multicolor quantum dots. *Nano lett.* **9**, 2199–2205.

Betzig, E., Patterson, G.H., Sougrat, R., *et al.* (2006) Imaging intracellular fluorescent proteins at nanometre resolution. *Science* **313**, 1642–1645.

Bornfleth, H., Satzler, K., Eils, R. & Cremer, C. (1998) High-precision distance measurements and volume-conserving segmentation of objects near and below the resolution limit in three-dimensional confocal fluorescence microscopy. *J. Microsc.* **189**, 118–136.

Churchman, L., Ökten, Z., Rock, R., Dawson, J. & Spudich, J. (2005) Single molecule high-resolution colocalization of Cy3 and Cy5 attached to macromolecules measures intramolecular distances through time. *Proc. Natl. Acad. Sci. U.S.A* **102**, 1419–1423.

Churchman, L.S., Flyvbjerg, H. & Spudich, J.A. (2006) A non-Gaussian distribution quantifies distances measured with fluorescence localization techniques. *Biophys. J.* **90**, 668–671. doi: 10.1529/biophysj.105.065599.

Dani, A., Huang, B., Bergan, J., Dulac, C. & Zhuang, X. (2010) Superresolution imaging of chemical synapses in the brain. *Neuron.* **68**, 843–856. doi: 10.1016/j.neuron.2010.11.021.

Edelstein, A., Amodaj, N., Hoover, K., Vale, R. & Stuurman, N. (2010) Computer control of microscopes using μ Manager. *Current Protocols in Molecular Biology*. New York, Green Publishing Associates and Wiley Interscience. doi: 10.1002/0471142727.mb1420s92.

Gibson, S.F. & Lanni, F. (1992) Experimental test of an analytical model of aberration in an oil-immersion objective lens used in three-dimensional light microscopy. *J. Opt. Soc. Am. a-Opt. Image Sci. Vision.* **9**, 154–166. doi: 10.1364/JOSAA.8.001601.

Goshtasby, A. (1988) Image registration by local approximation methods. *Image Vision Comput.* **6**, 255–261.

Gustafsson, M.G. (2000) Surpassing the lateral resolution limit by a factor of two using structured illumination microscopy. *J. Microsc.* **198**, 82–87.

Gustafsson, M.G., Agard, D.A. & Sedat, J.W. (1999) I5M: 3D widefield light microscopy with better than 100 nm axial resolution. *J. Microsc.* **195**, 10–16.

Hell, S.W., Schrader, M. & van der Voort, H.T. (1997) Far-field fluorescence microscopy with three-dimensional resolution in the 100-nm range. *J. Microsc.* **187**, 1–7.

Hell, S.W. & Wichmann, J. (1994) Breaking the diffraction resolution limit by stimulated emission: stimulated-emission-depletion fluorescence microscopy. *Opt. Lett.* **19**, 780–782.

Hoyer, P., Staudt, T., Engelhardt, J. & Hell, S.W. (2011) Quantum dot blueing and blinking enables fluorescence nanoscopy. *Nano Lett.* **11**, 245–250. doi: 10.1021/nl103639f.

Ji, N., Milkie, D.E. & Betzig, E. (2010) Adaptive optics via pupil segmentation for high-resolution imaging in biological tissues. *Nat. Methods*. **7**, 141–147. doi: 10.1038/nmeth.1411.

Joglekar, A.P., Bloom, K. & Salmon, E.D. (2009) In vivo protein architecture of the eukaryotic kinetochore with nanometer scale accuracy. *Curr. Biol.* **19**, 694–699. doi: 10.1016/j.cub.2009.02.056.

Kam, Z., Hanser, B., Gustafsson, M.G., Agard, D.A. & Sedat, J.W. (2001) Computational adaptive optics for live three-dimensional biological imaging. *Proc. Natl. Acad. Sci. U.S.A.* **98**, 3790–3795. doi: 10.1073/pnas.071275698.

Lacoste, T.D., Michalet, X., Pinaud, F., Chemla, D.S., Alivisatos, A.P. & Weiss, S. (2000) Ultrahigh-resolution multicolor colocalization of single fluorescent probes. *Proc. Natl. Acad. Sci. U.S.A.* **97**, 9461–9466. doi: 10.1073/pnas.170286097.

Manders, E. (1997) Chromatic shift in multicolour confocal microscopy. *J. Microsc.* **185**, 321–328.

Michalet, X., Lacoste, T.D. & Weiss, S. (2001) Ultrahigh-resolution colocalization of spectrally separable point-like fluorescent probes. *Methods.* **25**, 87–102. doi: 10.1006/meth.2001.1218.

Moree, B., Meyer, C.B., Fuller, C.J. & Straight, A.F. (2011) CENP-C recruits M18BP1 to centromeres to promote CENP-A chromatin assembly. *J. Cell Biol.* doi: 10.1083/jcb.201106079.

Mortensen, K.I., Churchman, L.S., Spudich, J.A. & Flyvbjerg, H. (2010) Optimized localization analysis for single-molecule tracking and super-resolution microscopy. *Nat. Methods.* **7**, 377–381. doi: 10.1038/nmeth.1447.

Nishikawa, S., Arimoto, I., Ikezaki, K., Sugawa, M., Ueno, H., Komori, T., Iwane, A.H. & Yanagida, T. (2010) Switch between large hand-over-hand and small inchworm-like steps in myosin VI. *Cell.* **142**, 879–888. doi: 10.1016/j.cell.2010.08.033.

Pertsinidis, A., Zhang, Y. & Chu, S. (2010) Subnanometre single-molecule localization, registration and distance measurements. *Nat.* **466**, 647–651. doi: 10.1038/nature09163.

Rust, M.J., Bates, M. & Zhuang, X. (2006) Sub-diffraction-limit imaging by stochastic optical reconstruction microscopy (STORM). *Nat. Methods.* **3**, 793–795. doi: 10.1038/nmeth929.

Schwertner, M., Booth, M. & Wilson, T. (2004a) Characterizing specimen induced aberrations for high NA adaptive optical microscopy. *Opt. Exp.* **12**, 6540–6552.

Schwertner, M., Booth, M.J., Neil, M.A.A. & Wilson, T. (2004b) Measurement of specimen-induced aberrations of biological samples using phase stepping interferometry. *J. Microsc.* **213**, 11–19. doi: 10.1111/j.1365-2818.2004.01267.x.

Schwertner, M., Booth, M.J. & Wilson, T. (2007) Specimen-induced distortions in light microscopy. *J. Microsc.* **228**, 97–102. doi: 10.1111/j.1365-2818.2007.01827.x.

Shao, L., Isaac, B., Uzawa, S., Agard, D.A., Sedat, J.W. & Gustafsson, M.G.L. (2008) I5S: wide field light microscopy with 100-nm-scale resolution in three dimensions. *Biophys. J.* **94**, 4971–4983. doi: 10.1529/biophysj.107.120352.

Staudt, T., Lang, M.C., Medda, R., Engelhardt, J. & Hell, S.W. (2007) 2,2'-thiodiethanol: a new water soluble mounting medium for high resolution optical microscopy. *Microsc. Res. Tech.* **70**, 1–9. doi: 10.1002/jemt.20396.

Thompson, R.E., Larson, D.R. & Webb, W.W. (2002) Precise nanometer localization analysis for individual fluorescent probes. *Biophys. J.* **82**, 2775–2783. doi: 10.1016/S0006-3495(02)75618-X.

Wan, X., O'Quinn, R.P., Pierce, H.L.,*et al.* (2009) Protein architecture of the human kinetochore microtubule attachment site. *Cell.* **137**, 672–684. doi: 10.1016/j.cell.2009.03.035.

Warshaw, D.M., Kennedy, G.G., Work, S.S., Krementsova, E.B., Beck, S. & Trybus, K.M. (2005) Differential labeling of myosin V heads with quantum dots allows direct visualization of hand-over-hand processivity. *Biophys. J.* **88**, L30–L32. doi: 10.1529/biophysj.105.061903.

Yildiz, A., Forkey, J.N., McKinney, S.A., Ha, T., Goldman, Y.E. & Selvin, P.R. (2003) Myosin V walks hand-over-hand: single fluorophore imaging with 1.5-nm localization. *Science.* **300**, 2061–2065. doi: 10.1126/science.1084398.